

# Angular Optical Transparency Induced by Photonic Topological Transitions in Metamaterials

Pengcheng Huo, Yuzhang Liang, Si Zhang, Yanqing Lu, and Ting Xu\*

Photonic topological transitions (PTTs) in metamaterials open a new realm of research with a number of interesting optical phenomena and provide an efficient route to manipulate light–matter interactions at nanoscale.

Here, it is shown that, by tailoring the topology of anisotropic metamaterial's equi-frequency surface, a narrow angular optical transparency window appears around the PTT frequency, which makes the metamaterial strongly discriminate the light based primarily on the angle of incidence. In experimental implementation, a large-scale nanowire metamaterial is fabricated by bottom-up approach and achieves a highly transparent window with a narrow angular range at visible frequency. Based on this angular transparency effect, the metamaterial is further demonstrated to be capable of significantly suppressing the diffraction and interference of the light scattered from arbitrarily shaped objects and projecting their diffraction-limited images into far field. These features make the metamaterials hold promise for a series of angle-dependent optical applications.

at constant frequency, EFS maps the angular dependence of wavevectors in the metamaterial and indicates the direction of power flow. Therefore, the topology of EFS directly governing the wave dynamics and the nature of light inside the metamaterial could have a dramatic change along with PTT. This opens a new route to efficiently manipulate light–matter interactions at nanoscales.

Here, we introduce a basic principle to generate an angular optical transparency in the metamaterial based on PTT. By engineering metamaterial's EFS from closed ellipsoid to an open hyperboloid, we find that a narrow angular optical transparency window appears around the transition point of PTT. As a result, the metamaterial exhibits strong angular discrimination of light: only the light very close to the normal incidence can be

## 1. Introduction

Metamaterials are artificial electromagnetic structures engineered on subwavelength scales to have optical properties that are not observed in their constituent materials and may not be found in nature, such as negative refractive index.<sup>[1–4]</sup> They have enabled unprecedented flexibility in manipulating light waves and producing various novel optical functionalities. Since the beginning of this century, with the development of nanofabrication and characterization technologies, there has been a tremendous growing interest in the study of metamaterials and their potential applications in different fields including super-resolution imaging,<sup>[5,6]</sup> optical sensing,<sup>[7–9]</sup> and electromagnetic cloaking.<sup>[10,11]</sup>

Recently, photonic topological transition (PTT) in metamaterials have generated considerable research interest.<sup>[12–16]</sup> Unlike the topological phase transition in condensed matter systems<sup>[17,18]</sup> and optical topological insulators,<sup>[19–21]</sup> here PTT only refers to the transition of topology of metamaterial's equi-frequency surface (EFS). As a surface of allowed wavevectors

well transmitted through the metamaterial with high transmission efficiency, while the light from other directions will be completely blocked. As experimental demonstration, for *p*-polarized incident light, we fabricate a large-area metamaterial slab consisting of metallic nanowires embedded in the dielectric matrix and achieve an angular window of transparency about  $\pm 4^\circ$  at the visible wavelength of 665 nm. Based on the angular transparency effect, we further demonstrate that the metamaterial slab can be used as a “flat-lens,” which is capable of projecting the diffraction-limited images of arbitrarily shaped, 2D objects into far field. Compared with other angularly selective material systems, like photonic crystals,<sup>[22,23]</sup> plasmonic nanogratings<sup>[24,25]</sup> and geometrical optics,<sup>[26,27]</sup> our designed metamaterial has a much narrower angular transparency window and single-layer planar architecture. These features make it very attractive for a series of applications, such as lensless on-chip imaging,<sup>[28]</sup> privacy protection,<sup>[29]</sup> and high-efficiency solar energy manipulation.<sup>[30]</sup>

## 2. Experimental Section

### 2.1. Sample Fabrication

The metamaterials are fabricated by filling silver nanowires in the highly ordered porous anodic aluminum oxide (AAO) templates. First, the high-purity aluminum foil (99.999%) is sequentially immersed in ethanol, acetone, and deionized water to remove impurities and organics of the surface. Electrochemical polishing is performed in the 4:1 mixed solution of perchloric acid and

Dr. P. Huo, Dr. Y. Liang, Dr. S. Zhang, Prof. Y. Lu, Prof. T. Xu  
National Laboratory of Solid State Microstructures, College of  
Engineering and Applied Sciences, Collaborative Innovation Center of  
Advanced Microstructures  
Nanjing University  
Nanjing 210093, China  
E-mail: xuting@nju.edu.cn

DOI: 10.1002/lpr.201700309

ethanol at 20 V and 10 °C to smooth the surface of the aluminum sheet. Then, we adopt the two-step anodization method to obtain AAO templates with uniform pores. A solution of 1.5 M sulfuric acid is used as the electrolyte solution for the first and second anodization. The first anodization of 6 h at 14 V and 10 °C can produce a sacrificial layer. After that, the irregular AAO layer is chemically etched by a mixture of 6 wt% phosphoric acid and 1.8 wt% chromic acid at 60 °C for 9 h. The second anodization is performed under the same conditions as the first anodization. The thickness of the AAO is controlled by the second anodizing time. A polymethyl methacrylate (PMMA) layer is coated on AAO from a PMMA/methylbenzene solution. Then, the Al substrate is detached in saturated SnCl<sub>4</sub>. The removal of the thin barrier layer was carried out in a solution of 5 wt% phosphoric acid for 30 min at 30 °C. The pore size of the AAO is controlled by the corrosion time in phosphoric acid. Subsequently, a thin layer of Au (thickness of ≈200 nm) is sputtered onto the open side of the AAO to serve as working electrode for the following electrodeposition process. The PMMA on the other side of the AAO template is thoroughly dissolved in the acetone solution. The template is finally transferred onto the ITO glass and follows to grow silver nanowires inside the nanopores. The electrolyte contains 0.06 mol L<sup>-1</sup> AgNO<sub>3</sub> and 0.5 mol L<sup>-1</sup> H<sub>3</sub>BO<sub>3</sub>. All of the chemical reagents used in this experiment are analytical grade. Potentiostatic deposition is carried out under DC conditions for dozens of minutes at room temperature and the constant potential is 0.6 V. The overgrown nanowires on the top surface and the thin Au layer on the bottom surface are removed by using chemical mechanical polishing and ion beam etching. Finally, the AAO membranes filled with silver nanowires are transferred onto transparent glass and Au mask substrate.

## 2.2. Optical Measurement

For the angular optical transparency measurement, a collimated, linear-polarized laser beam filtered from super-continuum laser is directly incident onto the metamaterial sample. The incident angle is controlled by the rotation stage. The intensity profiles of transmitted beam through the metamaterial slab are recorded by the charge coupled device (CCD) camera. For the imaging measurement, a circular-polarized laser beam is incident on the back-side of the opaque Au mask. FIB milling (Ga<sup>+</sup> ions, 30 kV, 40 pA) is used to pattern a 20 μm × 25 μm symbol “π” with slit aperture width of 200 nm. An optically inverted microscope with 50× objective lens focusing at different z positions is used to capture the objective image.

## 2.3. Numerical Simulation

Numerical simulations are performed by using finite-difference time-domain (FDTD) algorithm. The permittivity of AAO is  $\epsilon_{\text{Al}_2\text{O}_3} = 3.12$  for entire optical region of our interest.<sup>[31]</sup> By applying the Drude model, the permittivity of silver is described as follows:

$$\epsilon_{\text{Ag}}(\omega) = \epsilon_{\infty} - \frac{\omega_p^2}{\omega(\omega + i\gamma_c)}$$

Here the  $\epsilon_{\infty} = 6$  is the high-frequency permittivity of bulk silver, the  $\omega_p = 1.5 \times 10^{16}$  rad s<sup>-1</sup> is the bulk plasmon frequency, and  $\gamma_c = 7.73 \times 10^{13}$  rad s<sup>-1</sup> is the collision frequency, which all are obtained by fitting the model to the experimental data from the literature.<sup>[32]</sup> A transverse magnetic plane wave (magnetic field is polarized perpendicular to incident plane) is considered with an incident angle ranging from 0 to 90°. In the simulation, Bloch boundary conditions are applied along the x-axis and y-axis, and perfectly matched layers are used in the z-axis. The grid size along the x-, y-, and z-direction is 2 nm × 2 nm × 2 nm, respectively. The time-step size is  $2.7 \times 10^{-3}$  fs and the converged results are less than  $1 \times 10^{-5}$ .

## 3. Results and Discussions

### 3.1. Photonic Topological Transition and Angular Transparency in Anisotropic Medium

To demonstrate the fundamental physics principle at work here, we first start by considering a lossless, nonmagnetic anisotropic medium with relative permeability  $\mu = 1$  and a diagonal relative permittivity tensor  $\epsilon(\omega) = \text{Diag}\{\epsilon_x, \epsilon_y, \epsilon_z\}$ , where  $\epsilon_x = \epsilon_y = \epsilon_{\perp}$  and  $\epsilon_z = \epsilon_{\parallel}$  are respectively the permittivity components perpendicular and parallel to the axis of anisotropy along z-direction,  $\omega$  is the wave frequency. The EFS for extraordinary (p-polarized) electromagnetic waves propagating inside this medium is given by

$$\frac{k_x^2 + k_y^2}{\epsilon_{\parallel}} + \frac{k_z^2}{\epsilon_{\perp}} = \left(\frac{\omega}{c}\right)^2 \quad (1)$$

Here,  $k_x$ ,  $k_y$ , and  $k_z$  are respectively the components of the wavevector along x-, y-, and z-directions,  $c$  is the speed of light. Based on Equation (1), **Figure 1a** gives the calculated EFS for such medium with dispersive values of  $\epsilon_{\parallel}$  [ $\epsilon_{\parallel}(\omega) = 1, 0.1, 0, -0.1, -1$ ] while fixing  $\epsilon_{\perp} = 4$ . It can be clearly seen that on decreasing the value of  $\epsilon_{\parallel}$  from positive to negative, the topology of EFS transits from a closed ellipsoid ( $\epsilon_{\parallel} \epsilon_{\perp} > 0$ ) to an open hyperboloid ( $\epsilon_{\parallel} \epsilon_{\perp} < 0$ ) and the diameter of the projection of EFS in xy plane is proportional to the value of  $|\epsilon_{\parallel}|$ . The PTT occurs at the transition frequency  $\omega_0$ , where  $\epsilon_{\parallel}(\omega_0) = 0$ . This corresponds to the singularity of Equation (1) and the EFS degenerates to two points on z-axis. At this moment, the medium would act as a spatial frequency filter and only the electromagnetic waves with pure wavevectors along z-axis are allowed to propagate inside it.

As for the practicality, almost all reported anisotropic artificial media have intrinsic losses, especially at optical frequencies.<sup>[33,34]</sup> Therefore, it is important to evaluate the effect of absorption losses at the transition frequency  $\omega_0$ . Here we add a reasonable imaginary part for  $\epsilon_{\parallel}(\omega_0)$  as  $\epsilon_{\parallel}(\omega_0) = 0 + 0.1i$  while keeping  $\epsilon_{\perp}(\omega_0) = 4$ , and calculate the EFS for the complex  $k_z$ . In contrast to the ideal degenerated points on the z-axis for the lossless medium, the topology of EFS at  $\omega_0$  keeps a narrow hyperboloid in the presence of absorption losses (**Figure 1b**), similar to the dispersion of epsilon-near-zero (ENZ) media.<sup>[35–38]</sup> At first sight, it seems that the absorption losses from  $\epsilon_{\parallel}$  are completely unhelpful for narrowing the angular transparency window because, under this condition, light waves with small transverse wavevectors

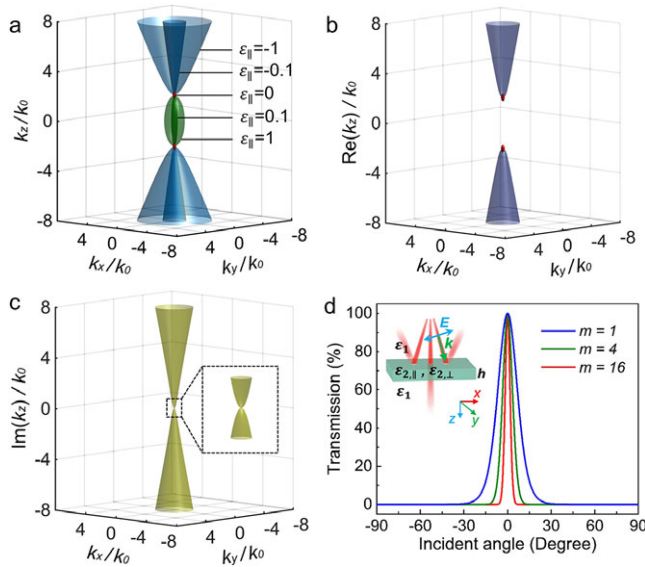


**Figure 1.** Photonic topological transitions in anisotropic material. a) Calculated EFS for the anisotropic material with dispersive values of  $\varepsilon_{||}$  [ $\varepsilon_{||}(\omega) = 1, 0.1, 0, -0.1, -1$ ] while fixing  $\varepsilon_{\perp} = 4$ . b–c) Calculated EFS with  $\varepsilon_{||} = 0 + 0.1i$  and  $\varepsilon_{\perp} = 4$  for b)  $\text{Re}(k_z)$  and c)  $\text{Im}(k_z)$  as a function of  $k_x$  and  $k_y$ . The inset in (c) shows a triply degenerate state existing at the origin. d) Calculated optical transmission as a function of incident angle  $\theta$  with different thicknesses  $h$ . Inset: Schematic diagram of the  $p$ -polarized light incident from isotropic surrounding medium onto the anisotropic material slab with thickness  $h$  at different incident angles.

are also supported to propagate inside the medium. However, situation is different if we take into account the imaginary part of  $k_z$ . As shown in Figure 1c, wavevector diagram for the imaginary part of  $k_z$  as a function of  $k_x$  and  $k_y$  exhibits a conical dispersion. The conical dispersion achieves a triply degenerate state at the origin and forms a *Dirac*-like point. This indicates that the light waves with pure wavevectors along  $z$ -direction have  $\text{Im}(k_z) = 0$  and do not experience any absorption losses in the medium. On the other side, for the light waves with small transverse wavevectors, the component  $\text{Im}(k_z) \neq 0$ , which means they do suffer from the material's intrinsic losses and the energy will decay with further propagation inside the medium. Therefore, although the topology of EFS in presence of the loss for  $\varepsilon_{||}$  at the transition point will diverge from two points to hyperboloid, the loss itself also can be helpful for suppressing the waves propagating away from  $z$ -direction and keeping a narrow angular transparency window.

Next, let us consider a practical application scenario where a slab of such anisotropic medium [ $\varepsilon_{\perp}(\omega_0) = 4$ ,  $\varepsilon_{||}(\omega_0) = 0 + 0.1i$ ] with thickness  $h$  is embedded in a surrounding medium with an isotropic relative permittivity  $\varepsilon_1$ , such as air. A  $p$ -polarized light at wave frequency  $\omega_0$  is incident from the surrounding medium onto the anisotropic medium slab at an incident angle  $\theta$ , as shown in inset of Figure 1d. Here we only consider  $p$ -polarized light because the EFS of non-magnetic anisotropic medium with  $\mu = 1$  does not experience PTT for  $s$ -polarization. According to the continuity of phase and

conservation of energy at two interfaces, the optical transmission of the incident light through the slab is given as

$$T = \left| \frac{4ak_{1z}k_{2z}\varepsilon_{\perp}\varepsilon_1}{(k_{1z}\varepsilon_{\perp} + k_{2z}\varepsilon_1)^2 - (k_{1z}\varepsilon_{\perp} - k_{2z}\varepsilon_1)^2 a^2 \exp(-i\delta)} \right|^2 \quad (2)$$

where  $k_{1z}$  and  $k_{2z}$  are the wavevector along  $z$ -axis in the surrounding isotropic medium and anisotropic medium, respectively; transmission loss  $a = \exp[-\text{Im}(k_{2z})h]$  and phase factor  $\delta = \text{Re}(k_{2z}) \cdot 2h$ . For the normal incidence ( $\theta = 0$ ), when the thickness of the anisotropic medium slab satisfies the condition  $h = m\pi/\omega_0\sqrt{\varepsilon_{\perp}}$  ( $m$  is a non-zero positive integer),  $T$  reaches the maximum for 1. Unlike other angular selectivity systems which have a strict index-matching requirement between the functional and environmental media to achieve high optical transmission,<sup>[22,23]</sup> here the maximum transmission is insensitive to the dielectric constant  $\varepsilon_1$  of the surrounding medium, which greatly extends the application range of the anisotropic medium. Based on Equation (2), Figure 1d displays the calculated optical transmission as a function of incident angle  $\theta$  with different slab thickness  $h$ . It can be seen that at  $\theta = 0$ , although  $T = 1$  for all the thickness  $h$  ( $m = 1, 4, 16$ ), a thicker slab has a narrower angular transparency window. These results agree well with the conclusion we obtained above that the intrinsic loss from  $\varepsilon_{||}$  in anisotropic medium will suppress the waves propagating away from  $z$ -direction. Therefore, without affecting the optical transmission for normal incidence, the width of the angular transparency window can be controlled by choosing proper slab thickness.

### 3.2. Experimental Realization of PTT-Based Angular Transparency Using Metamaterials

In order to show the feasibility of the angular optical transparency described above, we present an experimental realization at visible frequencies using a low-loss nanowire metamaterial structure which has been explored for optical nonlocality,<sup>[15,36]</sup> negative refraction,<sup>[39,40]</sup> and enhanced Purcell factor.<sup>[41]</sup> The metamaterial is formed by embedding arrays of parallel Ag nanowires with hexagonal lattice in a dielectric matrix ( $\text{Al}_2\text{O}_3$ ), as shown in Figure 2a. Supposing the geometric parameters, including nanowires radius  $r$  and lattice constant  $S$ , are much smaller than the operating wavelength  $\lambda_0$ , the metamaterial system can be treated as an effective anisotropic medium based on the effective medium theory.<sup>[42]</sup> The effective permittivity tensor of the metamaterial takes the form as  $\varepsilon_z = \varepsilon_{||} = f\varepsilon_{\text{Ag}} + (1-f)\varepsilon_{\text{Al}_2\text{O}_3}$  and  $\varepsilon_x = \varepsilon_y = \varepsilon_{\perp} = \varepsilon_{\text{Al}_2\text{O}_3} [(1+f)\varepsilon_{\text{Ag}} + (1-f)\varepsilon_{\text{Al}_2\text{O}_3}] / [(1+f)\varepsilon_{\text{Al}_2\text{O}_3} + (1-f)\varepsilon_{\text{Ag}}]$ , where  $\varepsilon_{\text{Ag}}$  and  $\varepsilon_{\text{Al}_2\text{O}_3}$  are the dielectric constants of the Ag and  $\text{Al}_2\text{O}_3$ , respectively, and  $f$  is the filling fraction of Ag. Figure 2b gives the calculated effective complex permittivities,  $\varepsilon_{||}$  and  $\varepsilon_{\perp}$ , of the metamaterial with  $f = 0.124$  (corresponding to  $r = 12$  nm and  $S = 65$  nm) in the visible region. It can be seen that the real part of  $\varepsilon_{||}$  continuously changes from positive to negative with increasing the wavelength and has  $\text{Re}(\varepsilon_{||}) = 0$  at  $\lambda_0 = 675$  nm. In contrast,  $\text{Re}(\varepsilon_{\perp})$  keeps positive in the entire investigated wavelength range. Therefore, the topology of

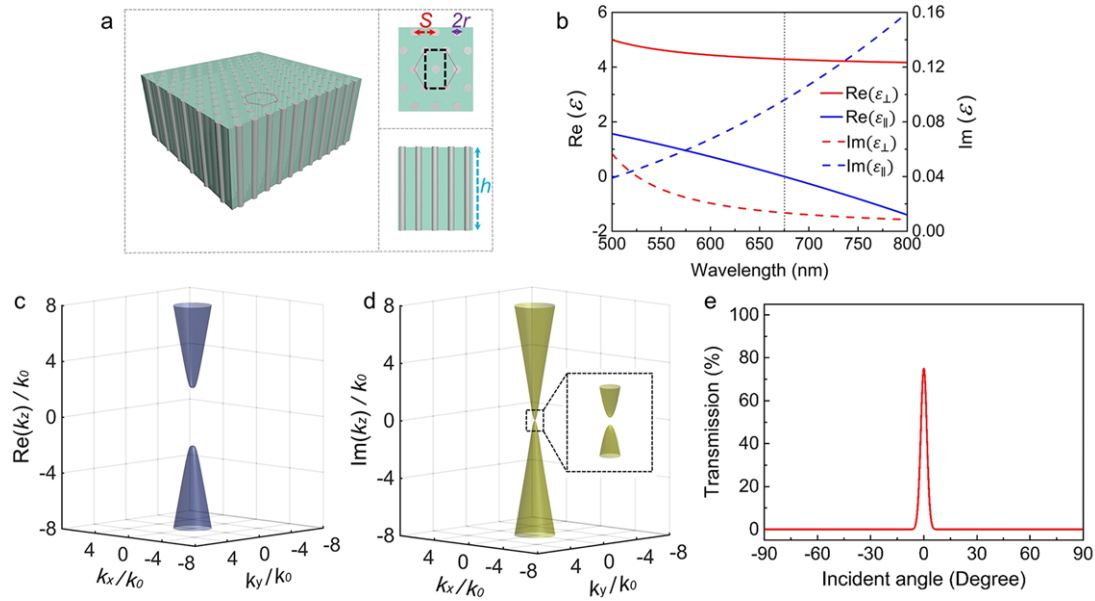


**Figure 2.** Realization of photonic topological transitions in metamaterial. a) Schematic diagram of the metamaterial in which metallic nanowires are embedded in a dielectric matrix. The radius of the nanowire is  $r$  and the center-to-center distance between two neighboring nanowires (lattice constant) is  $S$ , which generates a nanowire volume filling fraction  $f = 2\pi r^2/(\sqrt{3}S^2)$ . The thickness of the metamaterial slab is  $h$ . b) Calculated effective permittivity  $\varepsilon_{\parallel}$  and  $\varepsilon_{\perp}$  for metamaterial with filling fraction  $f = 0.124$ . The dashed line indicates the wavelength position (675 nm), where  $\varepsilon_{\parallel} = 0$ . c–d) Calculated EFS for c)  $\text{Re}(k_z)$  and d)  $\text{Im}(k_z)$  as a function of  $k_x$  and  $k_y$  at the wavelength of 675 nm. The inset in (d) shows a bandgap existing around the origin. e) Numerically simulated optical transmission of a 2.6  $\mu\text{m}$  thick metamaterial at the wavelength of 675 nm.

metamaterial's dispersion transits from a closed ellipsoid to an open hyperboloid at the transition wavelength  $\lambda_0 = 675$  nm. Based on the obtained effective anisotropic permittivities at  $\lambda_0$ , we calculate the metamaterial's EFS for the complex wavevector  $k_z$ , as shown in Figure 2c,d. Similar to the Figure 1b, the topology of the metamaterial's EFS for  $\text{Re}(k_z)$  at  $\lambda_0$  keeps a narrow hyperboloid, which indicates the metamaterial has a narrow angular transparency window. But in contrast to a triply degenerate Dirac-like point shown in Figure 1c, the metamaterial's EFS for  $\text{Im}(k_z)$  is different at the origin. It opens a bandgap due to the existence of the imaginary part of  $\varepsilon_{\perp}$ . As a result, even the light with pure wavevectors along  $z$ -axis would experience some absorption losses. Figure 2d gives the FDTD-simulated optical transmission of  $p$ -polarized incident light as function of  $\theta$  for a nanowire metamaterial slab surrounded by the air at  $\lambda_0 = 675$  nm, where the thickness of the slab is set to  $h = 2.6$   $\mu\text{m}$  ( $\approx 3.85\lambda_0$ ), satisfying the condition of transmission maximum ( $h = m\pi/\omega_0\sqrt{\varepsilon_{\perp}}$ ,  $m = 16$ ). The transparency window has an angular full width at half maximum (FWHM) of  $4^\circ$  ( $-2^\circ < \theta < 2^\circ$ ) with an optical transmission higher than 75% at  $\theta = 0$ , which indicates that the nanostructured metamaterial has comparable optical performances as the ideal anisotropic medium we proposed above.

Above nanowire metamaterial design is based on the local effective medium theory. Actually, the nonlocality in nanowire structures often leads to the appearance of the additional longitudinal resonance and results in a slight deviation of the real part of  $\varepsilon_{\parallel}$  from zero in the ENZ regime.<sup>[15,36]</sup> Nevertheless, in the designed thick metamaterial slab ( $h \approx 3.85\lambda_0$ ), even the real part of  $\varepsilon_{\parallel}$  is not zero, the waves propagating away from the normal direction will be suppressed by the absorption loss due

to the existence of the imaginary part of  $\varepsilon_{\parallel}$  ( $\approx 0.1i$ ). Therefore, the nonlocality in nanowire metamaterial does not have a big influence on the angular transparency effect.

A large-scale metamaterial sample is fabricated by electrochemical deposition of Ag nanowires in the highly ordered porous AAO membranes created by anodization. **Figure 3a** shows the optical image of a 2.6  $\mu\text{m}$  thick nanowire metamaterial slab transferred on the glass substrate. The metamaterial has an average Ag nanowire diameter  $d = 24$  nm and lattice constant  $S = 65$  nm. These critical geometric parameters are much smaller than the previously reported nanowire metamaterials operating at similar frequencies,<sup>[39,40]</sup> which is beneficial for more accurate approximation of the metamaterial's electromagnetic responses described by the effective medium theory. To characterize the optical performance, the metamaterial sample is illuminated with  $p$ -polarized, wavelength-filtered white laser with different incident angles. The transmitted light is collected and imaged by an angle-resolved experimental setup with angular resolution of  $1^\circ$ . Figure 3b shows the recorded optical images of the collimated laser beam transmitted through the metamaterial sample with different incident angles at  $\lambda = 665$  nm. Compared with a bright spot taken from the transmitted beam at  $\theta = 0$ , intensities of the transmitted beam spots decay rapidly with increasing  $\theta$ . When  $\theta > 10^\circ$ , the incident light is almost completely blocked by the metamaterial, which implies that the metamaterial slab has a good angular selectivity performance along the normal direction. Figure 3c gives the measured angular optical transmission  $T$  as a function of both incident angle and free-space wavelength ( $\lambda$  ranging from 625 to 725 nm). The narrowest transparency window with FWHM =  $8^\circ$  ( $-4^\circ < \theta < 4^\circ$ ) and optical transmission  $T = 62\%$  occurs at  $\lambda = 665$  nm.

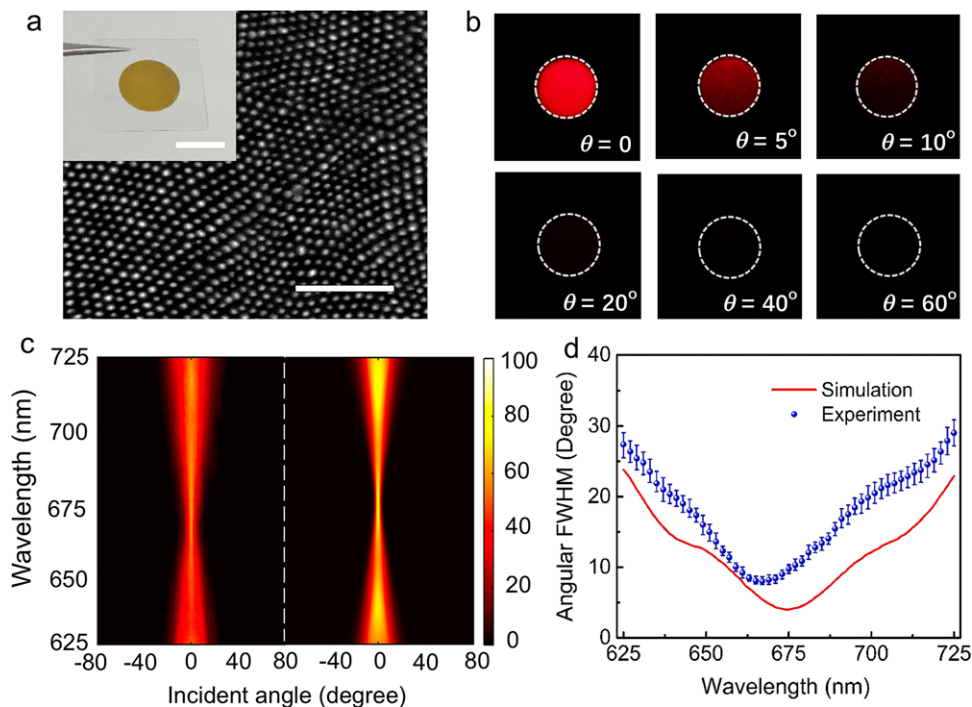


**Figure 3.** Angular optical transparency in metamaterials. a) Scanning electron microscope (SEM) images of the fabricated nanowire metamaterial. Scale bar, 500 nm. Left inset: glass slide uniformly coated with 2.6  $\mu\text{m}$  thick metamaterial. Scale bar: 2 cm. b) Charge-coupled device (CCD) recorded intensity profiles of the *p*-polarized, collimated light beam transmitted through metamaterial with different incident angle  $\theta$ . The wavelength of incident light is 665 nm and the diameter of beam spot is about 1 mm. c) Experimentally measured (left) and numerically simulated (right) optical transmission as a function of free-space wavelength and incident angle. d) Angular FWHM of the optical transparency window for the metamaterial extracted from measured and simulated results. Error bars: standard deviation for four repeated experimental measurements.

These results agree with the FDTD predictions, in which the narrowest transparency window has FWHM =  $4^\circ$  ( $-2^\circ < \theta < 2^\circ$ ) at  $\lambda = 675$  nm. The small differences between experimental and simulated results may come from the dimensional or morphological deviations in the structure of the fabricated sample compared with that of the ideal model structure.

Although in principle the transition point of PTT just corresponds to a single working frequency, but actually the metamaterial shows a broadband angular optical transparency effect. Figure 3d summarizes the angular FWHM of transparency window extracted from Figure 3c. In experiment, the wavelength span corresponding to an angular FWHM narrower than  $20^\circ$  ( $-10^\circ < \theta < 10^\circ$ ) is about 70 nm. This wavelength span is even boarder in simulation. The relatively board wavelength bandwidth for angular optical transparency is also enabled by the small intrinsic losses in nanowire metamaterial: Even the wave frequency deviates from the transition frequency of PTT and its EFS transits to an ellipsoid or hyperboloid; the intrinsic losses in metamaterial would help to suppress the light waves propagating along other directions.

### 3.3. Projecting Diffraction-Limited Images Based on Angular Transparency

Since the metamaterial has a good angular transparency performance close to normal, we further explorer its potentials in the

application of far-field projection imaging for arbitrarily shaped, 2D objects. The schematic diagram is shown in Figure 4a, where a 2.6  $\mu\text{m}$  thick nanowire metamaterial slab is transferred on an opaque Ag film prepatterned with several apertures forming an objective symbol “ $\pi$ ” by focused-ion-beam (FIB) milling. The aperture width is set to a constant value of 200 nm to suppress the transmitted *s*-polarized light. As a reference, an opaque Ag film with same patterns but without metamaterial covering is also investigated (Figure 4b). A circularly polarized illumination at  $\lambda = 665$  nm is used to probe evenly all radial directions of each object. The resulting projected images of “ $\pi$ ” are shown in Figure 4a,b, as recorded by the optical microscope focused at different *z* position. For the metamaterial covering sample, due to the narrow angular transparency window of the metamaterial, the diffraction and scattering of light from each aperture are remarkably suppressed. As a result, the diffraction-limited objective contour can be projected and well maintained over distances longer than 10  $\mu\text{m}$ . By comparison, the control sample without metamaterial can only keep the objective contour clearly for about 3  $\mu\text{m}$ . After that distance, the diffraction and interference of the transmitted light completely blur the projection image. These results imply that the nanowire metamaterial is a good potential candidate to alleviate the diffraction effect and significantly improve imaging quality for the lensless imaging technology. It should be noted that this metamaterial projection procedure is different from metamaterial hyperlens imaging.<sup>[6]</sup> In that case, the hyperbolic metamaterials are deliberately

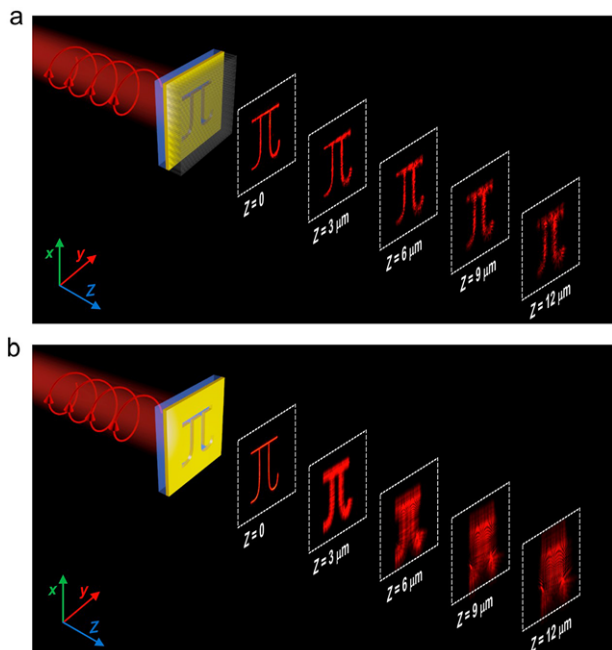


**Figure 4.** Projecting 2D object's image into far field. Optical images of the object patterned in the opaque Au film a) with and b) without metamaterial coating. The objective symbol " $\pi$ " has the aperture slit width 200 nm. The incident light at the wavelength of 665 nm is in circularly polarization and the images are recorded using an optical microscope focused at different z positions ( $z = 0$  corresponding to the exit surface of the Au film).

designed to support the propagation of a wide range of spatial frequency components, corresponding to a very large diameter of the projection of EFS in  $xy$  plane, totally contrary to the current case. Therefore, although the hyperbolic metamaterial lens can achieve sub-diffraction-limited imaging in the near field, the image quality would deteriorate rapidly away from the lens surface, similar to above control structure without metamaterial coating.

#### 4. Conclusions

In summary, we investigate the photonic topological transitions in anisotropic medium and present a general method to achieve angular optical transparency around the transition point. As a proof-of-concept demonstration, by tailoring the equifrequency surface, we design and fabricate a large-scale, low-loss anisotropic metamaterial consisting of metallic nanowires array by the electrochemical deposition approach. As expected, the metamaterial exhibits a narrow angular transparency window at visible frequencies. Consequently, we further explore its potentials in diffraction-limited far-field projection imaging of arbitrarily shaped, 2D objects. The single layer planar architecture associated with low-cost, bottom-up nanofabrication approach make this type of metamaterial very promising for building large-area optical platform for manipulating light propagation in a series of angle-dependent applications.

#### Acknowledgements

The work is supported by the Key Research and Development Program from Ministry of Science and Technology of China (2016YFA0202100 and 2017YFA0303700) and National Natural Science Foundation of China (61575092). The authors acknowledge support from the Thousand Talents Program for Young Professionals, Collaborative Innovations Center of Advanced Microstructures.

#### Conflict of Interest

The authors declare no conflict of interest.

#### Keywords

angular transparency, metamaterials, photonic topological transition, surface plasmon

Received: November 13, 2017

Revised: April 4, 2018

Published online:

- [1] R. A. Shelby, D. R. Smith, S. Schultz, *Science* **2001**, 292, 77.
- [2] V. M. Shalaev, *Nat. Photon.* **2007**, 1, 41.
- [3] J. Valentine, S. Zhang, T. Zentgraf, E. Ulin-Avila, D. A. Genov, G. Bartal, X. Zhang, *Nature* **2008**, 455, 376.
- [4] T. Xu, A. Agrawal, M. Abshin, K. Chau, H. Lezec, *Nature* **2013**, 497, 470.
- [5] Z. Jacob, L. V. Alekseyev, E. Narimanov, *Opt. Express* **2006**, 14, 8247.
- [6] Z. Liu, H. Lee, Y. Xiong, C. Sun, X. Zhang, *Science* **2007**, 315, 5819.
- [7] A. V. Kabashin, P. Evans, S. Pastkovsky, W. Hendren, G. A. Wurtz, R. Atkinson, R. Pollard, V. A. Podolskiy, A. V. Zayats, *Nat. Mater.* **2009**, 8, 867.
- [8] N. Liu, M. Hentschel, T. Weiss, A. P. Alivisatos, H. Giessen, *Science* **2011**, 332, 1407.
- [9] Y. Zhao, A. N. Askarpour, L. Sun, J. Shi, X. Li, A. Alù, *Nat. Commun.* **2017**, 8, 14180.
- [10] D. Schurig, J. J. Mock, B. J. Justice, S. A. Cummer, J. B. Pendry, A. F. Starr, D. R. Smith, *Science* **2006**, 314, 977.
- [11] W. Cai, U. K. Chettiar, A. V. Kildishev, V. M. Shalaev, *Nat. Photon.* **2007**, 1, 224.
- [12] H. N. Krishnamoorthy, Z. Jacob, E. Narimanov, I. Kretzschmar, V. M. Menon, *Science* **2012**, 336, 205.
- [13] J. S. Gomez-Diaz, M. Tymchenko, A. Alù, *Phys. Rev. Lett.* **2015**, 114, 233901.
- [14] P. N. Dyachenko, S. Molesky, A. Y. Petrov, M. Störmer, T. Krekeler, S. Lang, M. Ritter, Z. Jacob, M. Eich, *Nat. Commun.* **2016**, 7, 11809.
- [15] P. Ginzburg, D. J. Roth, M. E. Nasir, P. Segovia, A. V. Krasavin, J. Levitt, L. M. Hirvonen, B. Wells, K. Suhling, D. Richards, V. A. Podolskiy, *Light Sci. Appl.* **2017**, 6, 6.
- [16] A. V. Shchelokova, D. S. Filonov, P. V. Kapitanova, P. A. Belov, *Phys. Rev. B* **2014**, 90, 115155.
- [17] I. M. Lifshitz, *Sov. Phys. JETP* **1960**, 11, 1130.
- [18] J. M. Kosterlitz, D. J. Thouless, *J. Phys. C* **1973**, 6, 1181.
- [19] S. Kruk, A. Slobozhanyuk, D. Denkova, A. Poddubny, I. Kravchenko, A. Miroshnichenko, D. Neshev, Y. Kivshar, *Small* **2017**, 13, 1603190.
- [20] L. Lu, J. D. Joannopoulos, M. Soljacic, *Nat. Photon.* **2014**, 8, 821.
- [21] W. Gao, M. Lawrence, B. Yang, F. Liu, F. Fang, B. Beri, J. Li, S. Zhang, *Phys. Rev. Lett.* **2015**, 114, 037402.
- [22] R. E. Hamam, I. Celanovic, M. Soljačić, *Phys. Rev. A* **2011**, 83, 035806.

- [23] Y. Shen, D. Ye, I. Celanovic, S. G. Johnson, J. D. Joannopoulos, M. Soljačić, *Science* **2014**, *343*, 1499.
- [24] A. Alù, G. D'Aguanno, N. Mattiucci, M. J. Bloemer, *Phys. Rev. Lett.* **2011**, *106*, 123902.
- [25] C. Argyropoulos, K. Q. Le, N. Mattiucci, G. D'Aguanno, A. Alù, *Phys. Rev. B* **2013**, *87*, 205112.
- [26] J. H. Atwater, P. Spinelli, E. Kosten, J. Parsons, C. Van Lare, J. Van de Groep, J. Garcia de Abajo, A. Polman, H. A. Atwater, *Appl. Phys. Lett.* **2011**, *99*, 15113.
- [27] E. D. Kosten, J. H. Atwater, J. Parsons, A. Polman, H. A. Atwater, *Light Sci. Appl.* **2013**, *2*, e45.
- [28] A. Greenbaum, W. Luo, T. W. Su, Z. Göröcs, L. Xue, S. O. Isikman, A. F. Coskun, O. Mudanyali, A. Ozcan, *Nat. Methods* **2012**, *9*, 889.
- [29] G. M. Clarke, P. D. Graham, B. R. Hansen, T. B. Hoium, D. F. Slama, *U.S. patent* **2008**, 7,467,873B2.
- [30] B. Roberts, D. M. Nanditha, M. Dissanayake, P. C. Ku, *Opt. Express* **2012**, *20*, 265.
- [31] E. D. Palik, *Handbook of Optical Constants of Solids*, Academic Press, Orlando **1985**.
- [32] P. B. Johnson, R. W. Christy, *Phys. Rev. B* **1972**, *6*, 4370.
- [33] C. M. Soukoulis, M. Wegener, *Nat. Photon.* **2011**, *5*, 523.
- [34] O. Hess, J. B. Pendry, S. A. Maier, R. F. Oulton, J. M. Hamm, K. L. Tsakmakidis, *Nat. Mater.* **2012**, *11*, 573.
- [35] B. Edwards, A. Alù, M. E. Young, M. Silveirinha, N. Engheta, *Phys. Rev. Lett.* **2008**, *100*, 033903.
- [36] R. J. Pollard, A. Murphy, W. R. Hendren, P. R. Evans, R. Atkinson, G. A. Wurtz, A. V. Zayats, V. A. Podolskiy, *Phys. Rev. Lett.* **2009**, *102*, 127405.
- [37] L. V. Alekseyev, E. E. Narimanov, T. Tumkur, H. Li, Y. A. Barnakov, M. A. Noginov, *Appl. Phys. Lett.* **2010**, *97*, 131107.
- [38] R. Maas, J. Parsons, N. Engheta, A. Polman, *Nat. Photon.* **2013**, *7*, 907.
- [39] Y. C. Liu, G. Bartal, X. Zhang, *Opt. Express* **2008**, *16*, 15439.
- [40] J. Yao, Z. Liu, Y. Liu, Y. Wang, C. Sun, G. Bartal, A. Stacy, X. Zhang, *Science* **2008**, *321*, 930.
- [41] A. P. Slobozhanyuk, P. Ginzburg, D. A. Powell, I. Iorsh, A. S. Shalin, P. Segovia, A. V. Krasavin, G. A. Wurtz, V. A. Podolskiy, P. A. Belov, A. V. Zayats, *Phys. Rev. B* **2015**, *92*, 195127.
- [42] V. M. Agranovich, V. E. Kravtsov, *Solid State Commun.* **1985**, *55*, 85.